AGU PUBLICATIONS

Geochemistry, Geophysics, Geosystems

RESEARCH ARTICLE

10.1002/2015GC005940

Key Points:

- Two modes of flat subduction: permanent underplating and transient flattening
- Cratonic lithosphere in the overriding plate produces highly contorted slab shapes
- Permanent underplating provides a built-in mechanism for regeneration of cratons

Supporting Information:

- Supporting Information S1
- Movie S1
- Movie S2
- Movie S3
- Movie S4
- Movie S5
- Movie S6

Correspondence to:
J. M. Taramón,
Jorge.TaramonGomez.2014@live.rhul.ac.uk

Citation:
Taramón, J. M., J. Rodríguez-González, A. M. Negredo, and M. I. Billen (2015), Influence of cratonic lithosphere on the formation and evolution of flat slabs: Insights from 3-D time-dependent modeling, *Geochem. Geophys. Geosyst.*, *16*, 2933–2948, doi:10.1002/2015GC005940.

Received 9 JUN 2015
Accepted 5 AUG 2015
Accepted article online 7 AUG 2015
Published online 6 SEP 2015

Influence of cratonic lithosphere on the formation and evolution of flat slabs: Insights from 3-D time-dependent modeling

Jorge M. Taramón[1,2], Juan Rodríguez-González[3], Ana M. Negredo[1], and Magali I. Billen[4]

[1]Department of Geophysics and Meteorology, Institute of Geosciences IGEO, Complutense University of Madrid, Madrid, Spain, [2]Now at Department of Earth Sciences, Royal Holloway University of London, UK, [3]Department of Geology, University of Maryland, College Park, Maryland, USA, [4]Department of Earth and Planetary Sciences, University of California-Davis, Davis, California, USA

Abstract Several mechanisms have been suggested for the formation of flat slabs including buoyant features on the subducting plate, trenchward motion and thermal or cratonic structure of the overriding plate. Analysis of episodes of flat subduction indicate that not all flat slabs can be attributed to only one of these mechanisms and it is likely that multiple mechanisms work together to create the necessary conditions for flat slab subduction. In this study we examine the role of localized regions of cratonic lithosphere in the overriding plate in the formation and evolution of flat slabs. We explicitly build on previous models, by using time-dependent simulations with three-dimensional variation in overriding plate structure. We find that there are two modes of flat subduction: permanent underplating occurs when the slab is more buoyant (shorter or younger), while transient flattening occurs when there is more negative buoyancy (longer or older slabs). Our models show how regions of the slab adjacent to the subcratonic flat portion continue to pull the slab into the mantle leading to highly contorted slab shapes with apparent slab gaps beneath the craton. These results show how the interpretation of seismic images of subduction zones can be complicated by the occurrence of either permanent or transient flattening of the slab, and how the signature of a recent flat slab episode may persist as the slab resumes normal subduction. Our models suggest that permanent underplating of slabs may preferentially occur below thick and cold lithosphere providing a built-in mechanism for regeneration of cratons.

1. Introduction

Flat slabs are characterized by a portion of the subducting plate, landward of the subducting-overriding plate interface, that develops a slab dip of less than ~5 degrees over a distance of greater than 100 km. Truly flat slabs are distinguished from shallow-dipping slabs by the complete loss of volcanic activity on the overriding plate. Presently, flat slabs in oceanic-continental subduction zones exist beneath central southern Alaska [*Bruns*, 1985], Mexico, Peru, and Chile (see references below). Past flat slab events are also inferred from the geologic record, such as the Laramide flat slab [*Humphreys*, 1995; *Jones et al.*, 2011], and its northern extension, the Siletzia flat slab [*Darold and Humphreys*, 2013] in North America.

Several mechanisms have been proposed to cause flat-slab subduction including subduction of a buoyant feature [*Vogt*, 1973; *Cloos*, 1993; *Gutscher et al.*, 2000; *Espurt et al.*, 2008] and trenchward motion of the overriding plate [*Cross and Pilger*, 1982]. However, application of just one of these mechanisms to explain all flat slabs fails because [see also *Skinner and Clayton*, 2013]: (1) a single necessary condition does not exist for all the observed flat slabs, (2) there are counter examples in which the same conditions do not lead to flat slabs, or (3) dynamical simulations indicate that the proposed mechanism is insufficient to cause flat slab subduction.

For example, subduction of the buoyant Nazca ridge has been proposed for the Peru flat slab [*Gutscher et al.*, 1999; *Anderson et al.*, 2007], but no such feature is thought to exist to cause the flat slab in Central Mexico. In addition, numerical modeling has shown that buoyant features must have a large spatial extent and thick crust in order to cause significant flattening [*Martinod et al.*, 2005; *Gerya et al.*, 2009; *Arrial and Billen*, 2013; *Betts et al.*, 2015]. Therefore, models proposing that two large oceanic plateaus caused the long-lived (90–65 Ma) Laramide flat slab [*Saleeby*, 2003; *Liu et al.*, 2010] are consistent with dynamical constraints. However, it is difficult to reconcile dynamical models with the proposal that the much smaller Nazca ridge is solely responsible for the flat slab in Peru [*Skinner and Clayton*, 2013].

Similarly, trenchward motion of the overriding plate is observed or inferred for the Chilean and Peruvian flat slabs [*Vlaar*, 1983; *van Hunen et al*., 2000], but there are many other locations with similar rates of trenchward overriding plate motion that do not have flat slabs [*Schellart et al*., 2008]. In this case as well, 2-D numerical models have shown that trenchward motion of the overriding plate alone is insufficient to cause slab flattening unless the overriding plate is quite thick ($>$ 200–300 km) [*Manea et al*., 2012] or the trench retreat rate is high ($>$ 4 cm/yr) [*van Hunen et al*., 2000; *Cizkova et al*., 2002]. However, 3-D time-dependent flow models of recent ($<$ 20 Ma) subduction beneath North America indicate that trenchward overriding plate motion can cause transient episodes of slab flattening and segmentation of the slab resulting in complex 3-D slab morphology in the upper mantle [*van der Lee and Nolet*, 1997; *Liu and Stegman*, 2011]. In order to reconcile the observations of flat slabs with possible mechanisms and the constraints imposed by dynamical simulations, the structure of the overriding plate has been increasingly recognized as an additional factor that can contribute to flat slab subduction [*O'Driscoll et al*., 2009, 2012; *Capitanio et al*., 2010; *Roda et al*., 2011; *Rodríguez-González et al*., 2012, 2014]. For example, the flat slab region in central Mexico [*Pardo and Suarez*, 1995] is beneath a cold/thick region of the north American continent (i.e., the Maya Block) [*Blackwell and Richards*, 2004; *Artemieva*, 2006] and the Peru and Chilean flat slabs are both in close proximity to regions with large elastic plate thickness [*Tassara et al*., 2006; *Pérez-Gussinyé et al*., 2008; *Tassara and Echaurren*, 2012]. Furthermore it has been proposed that rather than subduction of oceanic plateaus, initial shallowing of the Farallon slab beneath North America was caused by an increase in trenchward motion of the overriding plate and the Laramide flat slab formed due to subsequent interaction with the Wyoming Craton [*Jones et al*., 2011].

The physical mechanism by which variable overriding plate thickness can cause flat slabs is flow-induced reduction in pressure within the mantle wedge [*Stevenson and Turner*, 1977]: narrowing of the mantle wedge or increasing the wedge viscosity both act to increase negative pressure and pull the slab upward. This upward pull by the hydrodynamic stresses is often termed "suction." For shallow-dipping slabs this suction provides a positive feedback for which slabs continue to shallow once they have reached a critically shallow dip. Similarly, once the slab dip has steepened beyond a critically steep dip, it will continue to steepen. The critical dip in both cases depends on the details of the slab negative buoyancy, the viscosity of the mantle and the rate of subduction.

Three-dimensional instantaneous flow models show that a thick cratonic root can increase the magnitude of suction acting on the subducting plate due to mantle-wedge flow and that this suction effect will vary along strike if the craton has a finite width [*O'Driscoll et al*., 2009, 2012]. Specifically, these models provide a strong indication that craton location in South America plays an important role in controlling slab dip and the formation of flat slabs through enhanced suction [*O'Driscoll et al*., 2012], but they do not address the time evolution of the slab in response to this enhanced pressure.

In 2-D and 3-D time-dependent models, the increased suction due to a cold/thick overriding lithosphere, which leads to a higher viscosity and narrower wedge corner, causes significant shallowing and even flat slab subduction depending on the age (buoyancy) of the subducting plate, distance between the cold/thick region and the trench, and the thickness of the overriding plate [*Rodríguez-González et al*., 2012, 2014]. However, as with the other mechanisms, it is unlikely that this mechanism alone is capable of explaining all observations of flat slabs, because as the slab penetrates deeper into the upper mantle the torque due to the weight of the slab is larger than the torque due to the suction in the mantle wedge and the slab steepens [*Rodríguez-González et al*., 2012].

The combined effects of multiple flattening mechanisms have been explored in a few studies. Time-dependent flow models, considering two-dimensional geometries, demonstrate that adding trenchward overriding plate motion to either the effects of a buoyant subducting plate [*van Hunen et al*., 2002] or a cratonic root on the overriding plate [*Manea et al*., 2012] can cause flat slab subduction. Other two-dimensional models show that the combination of trenchward motion of the overriding plate and high subduction velocity can lead to flat subduction [*Currie and Beaumont*, 2011]. A physically based conceptual model applied to the Peru flat slab concludes that with trenchward overriding plate motion and enhanced suction beneath the continent, a narrow buoyant ridge is capable of causing flat slab subduction

[*Antonijevic et al*., 2015]. However, previous numerical models incorporating cratonic lithosphere in the overriding plate consider either 2-D geometries [*Currie and Beaumont*, 2011; *Manea et al*., 2012] or 3-D instantaneous flow [*O'Driscoll et al*., 2009, 2012], and therefore the role of finite width cratons on time-dependent subduction evolution has not yet been investigated.

In this study we present 2-D and 3-D time-dependent, numerical simulations demonstrating the effect of cratonic regions within the overriding lithosphere on formation of flat slabs. These models build directly on the results of previous work in which the overriding plate was split into a thick region adjacent to normal-thickness lithosphere [*Rodríguez-González et al*., 2014]. In these previous 3-D dynamical models it was found that shallowing of the slab occurred beneath the thick lithosphere and differences in dip persisted as the slab sank deeper through the upper mantle. Notably, slab shallowing occurred in cases with and without toroidal flow around the slab, and for steeply dipping (75°) and more shallow-dipping (55°) proto-slabs. However, these previous models were focused on the effect of slab evolution on flow in the mantle and therefore did not fully explore the effects of overriding plate structure, and in particular what parameters are necessary to cause flat slab subduction.

In summary, existing observations and models provide a framework for better understanding flat slab subduction, in which a combination of factors act together to create the necessary conditions for the formation of flat slabs. This framework suggests that overriding plate structure is likely to play a significant role in the formation and eventual collapse of flat slabs. However, the effects of cratons within the overriding plate have not yet been fully characterized. In the models presented here, we focus only on the interaction of the slab with the overriding plate structure and craton: we explicitly do not include other factors that are thought to contribute to flat slab subduction. However, we will return to the overarching framework to discuss our results in the context of a combination of factors that act together to cause flat slab subduction.

2. Methodology

2.1. Numerical Methods

We employed time-dependent 2-D and 3-D thermo-mechanical simulations of kinematically and dynamically driven subduction to investigate the role of cratonic lithosphere in the overriding plate on subduction dynamics. Kinematically driven simulations are used for exploratory models in 2-D and to create the proto-slab for 3-D dynamically driven models. We use a version of the finite-element code CitcomS [*Zhong et al*., 2000; *Tan et al*., 2006] modified to account for upper mantle composite (strain accommodated by diffusion and dislocation) rheology [*Jadamec and Billen*, 2010]. The equations of conservation of mass, momentum and energy are solved for a 3-D incompressible fluid under the Boussinesq approximation:

$$\nabla \cdot \vec{u} = 0 \tag{1}$$

$$\nabla \cdot \tau - \nabla P + \rho \vec{g} = 0 \tag{2}$$

$$\frac{\partial T}{\partial t} + \vec{u} \cdot \nabla T = \kappa \nabla^2 T \tag{3}$$

where $\vec{u}$ is the velocity field, $\tau_{ij} = \eta \dot{\varepsilon}_{ij}$ is the deviatoric stress tensor (viscosity multiplied by strain rate tensor), P is the total pressure, ρ is the density, $g = 9.8$ m s^{-2} is the gravity acceleration, T is the temperature and $\kappa = 10^{-6}$ m^2 s^{-1} is the thermal diffusivity. Density is given by the simplified state equation $\rho = \rho_0(1-\alpha(T-T_0))$, where $\rho_0 = 3300$ kg m^{-3} is density at the reference mantle temperature $T_0 = 1400$°C, and $\alpha = 2{\cdot}10^{-5}$ K^{-1} is the thermal expansion coefficient.

2.2. Model Design

The 3-D modeled domain is a spherical tesseroid representing a subduction zone that includes a subducting and an overriding plate in which a cratonic portion can be imbedded (Figure 1). The model domain is 1500 km deep and extends 18° (~2000 km) in the latitudinal direction (parallel to trench) and 48.5° (~5400 km) in the longitudinal direction (perpendicular to trench). Subduction takes place from left (west) to right (east). Due to geometric symmetry in the latitudinal direction, only the northern half of the domain (0–9°) is simulated numerically and the results are reflected southward with respect to the equatorial cross section (latitude $\lambda = 0°$) for a total extent of 18° in the latitudinal direction.

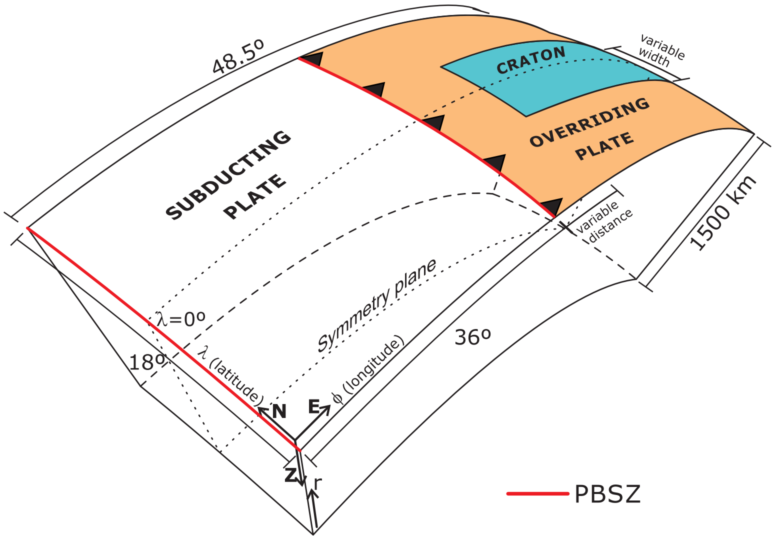

Figure 1. Model domain representing a 3-D spherical tesseroid that extends 1500 km in depth, 48.5° in longitude and 18° in latitude. The trench and overriding plate are fixed. The plate boundary shear zone is simulated by a low-viscosity channel (red line). Trench-craton distance, craton latitudinal extent, thermal thickness and length of the proto-slab vary from one model to another. See Table 1 for summary of 3-D model configurations.

The finite element grid has 161×163×641 nodes in the radial, latitudinal and longitudinal directions, respectively. Grid resolution ranges from 5 to 12 km in depth, 4 to 11 km in the longitudinal direction, and is uniform in the latitudinal direction with an element size of 10 km. The highest resolution is imposed in the area surrounding the plate boundary and the slab. In kinematically driven models we prescribe the velocity of the top boundary of the subducting plate (5–8 cm/yr) and the overriding plate (0 cm/yr), whereas the rest of the boundaries are free-slip; in dynamically driven models all of the model boundaries are free-slip. The top and bottom boundary temperatures are set at 0°C and 1400°C, respectively, and the lateral boundaries are thermally insulated.

The subducting plate is bounded to the west and east by a low viscosity zone, which simulates the plate boundaries. To the west, a vertical plate boundary simulated an oceanic spreading center and decouples the subducting plate from the model domain side-wall. The eastern boundary of the subducting plate (subduction hinge) decouples the overriding and subducting plates to allow for subduction. This imposed plate boundary shear zone (PBSZ) dips 30° and extends to a depth of 110 km. The reduced viscosity in the PBSZ approximates the different weakening mechanisms taking place at the plate boundary (e.g., shear heating, faulting, fracture or fluid release).

The PBSZ has a fixed location in space and therefore the trench cannot rollback or advance. We choose to have a fixed trench because (1) it significantly reduces the computational cost of the models, (2) the causes of trench motion are not fully understood [*Meyer and Schellart*, 2013; *Arredondo and Billen*, 2014; *Garel et al*., 2014; *Holt et al*., 2015] and (3) this choice allows us to examine the dynamics without the added complication of trench motion: we discuss the implication of this model design choice with respect to the simulation results.

2.3. Initial Temperature and Proto-Slab Structure

In the 3-D dynamically driven models, which are the main results presented, subduction is driven by the negative thermal buoyancy of a prescribed partially subducted slab (proto-slab). The proto-slab is created using kinematically driven simulations, and therefore its structure depends on the set-up and duration of these simulations (see supporting information). The initial thermal structure of the kinematically driven models is assigned according to a half-space cooling model (HSCM) [*Parker and Oldenburg*, 1973; *Schellart et al*., 2010]. The age of the subducting plate varies with the distance from the oceanic ridge at the western boundary. Given the extent in longitude of the subducting plate (36°) and the assumed convergence velocity, the age of the subducting plate varies from 0 Myr at the western boundary to 50 Myr at the subduction hinge. A uniform age is used for the overriding plate.

Table 1. Dynamically Driven 3-D Simulations Characteristics and Results

Model	Proto-Slab	Age of Subducting Plate (Myr)	Age of Overriding Plate (Myr)	Thermal Thickness of Craton (km)	Trench-Craton Distance	Craton Width	Coupling Slab-Overriding Plate
3D-E	Short	50	85				No
3D-F	Short	50	85	200 km	3°	6°	Yes
3D-G	Long	50	85	200 km	3°	6°	Transient
3D-H	Long	50	85	200 km	3°	9°	Yes
3D-I	Long	50	70	200 km	3°	6°	Transient

The thermal thickness of the overriding plate is obtained considering the lithosphere as the thermal boundary layer of a half-space cooling model, and using the expression $Z_T = 2.32\sqrt{\kappa t}$, where $\kappa = 10^{-6}$ m^2 s^{-1} is the thermal diffusivity and *t* is age (Z_T corresponds to $T = 0.9T_o$, or $T = 1260°C$) [*Turcotte and Schubert*, 2002]. For an age of 85 Myr, the thermal thickness is 120 km. We note that a half-space cooling model is not appropriate for modeling the detailed thermal structure of a craton, but is used here to generate a smoothly varying thermal structure that can be easily varied to obtain appropriate plate thickness for different regions of the model.

2.4. Rheology

The rheological model consists of a composite viscosity (olivine deformation accommodated by both dislocation and diffusion creep mechanisms) for the upper mantle [e.g., *van den Berg et al*., 1993; *Cizkova et al*., 2002; *Billen and Hirth*, 2007], a linear viscosity (diffusion creep) for the lower mantle and a yield stress (plastic viscosity) at cold temperatures. Specifically, we use the same rheological formulation (see supporting information) as in the previous study by *Jadamec and Billen* [2010]. The computed viscosity for each mechanism (diffusion and dislocation creep) at 250 km depth for a strain rate of 10^{-15} s^{-1} is equal and results in a composite viscosity of 10^{20} Pa·s. The choice of grain size in the lower mantle results in a one order of magnitude viscosity increase between the upper and lower mantle, in agreement with constraints from the geoid [*Hager*, 1984]. Maximum and minimum cut-off viscosities are 10^{24} Pa·s and 10^{19} Pa·s, respectively. The effective viscosity is limited by a pseudo-plastic mechanism with a maximum yield stress of 1 GPa.

The prescribed maximum viscosity in the PBSZ is 10^{21} Pa·s. However, the viscosity in the PBSZ is given by the minimum of the prescribed PBSZ maximum viscosity and the dynamically computed composite viscosity and therefore can be lower than this imposed value. The maximum value is chosen such that subduction velocities in dynamically driven models are on the order of 2–10 cm/yr.

3. Results

We first conducted a series of 2-D and 3-D kinematically driven simulations (see supporting information Tables S2 and S3, respectively). From previous studies we know that the general dynamic behavior of slabs in response to changes in the overriding plate structure is similar for both kinematically and dynamically driven subduction [*Rodríguez-González et al*., 2012, 2014] and so this provides a more efficient approach to exploring the parameter space. Next, based on the analysis of the kinematic model results, which we summarize below, we then conducted a smaller set of dynamically driven 3-D models of subduction with a craton (Table 1). From these dynamically driven simulations, Models 3D-F and 3D-G illustrate distinct styles of slab-craton interaction: a permanently underplated flat slab and a transient flat slab, respectively.

3.1. Kinematically Driven Models

Previous research into the effect of the overriding plate structure on the subducting slab dip demonstrates that a smaller opening angle of the mantle wedge (i.e., smaller slab dip), larger subduction velocity, and higher mantle viscosity promote shallowing of the slab by increasing the magnitude of the negative pressure above the slab (i.e., hydrodynamic suction) [*Stevenson and Turner*, 1977; *Rodríguez-González et al*., 2012, 2014]. In agreement with those predictions, using 2-D and 3-D kinematically driven models we find that a relatively cold overriding plate, thick cratons, reduced slab/craton distance, and higher subduction velocity, favor a shallower dip angle (see supporting information). Similarly, young slabs subduct at shallower angles

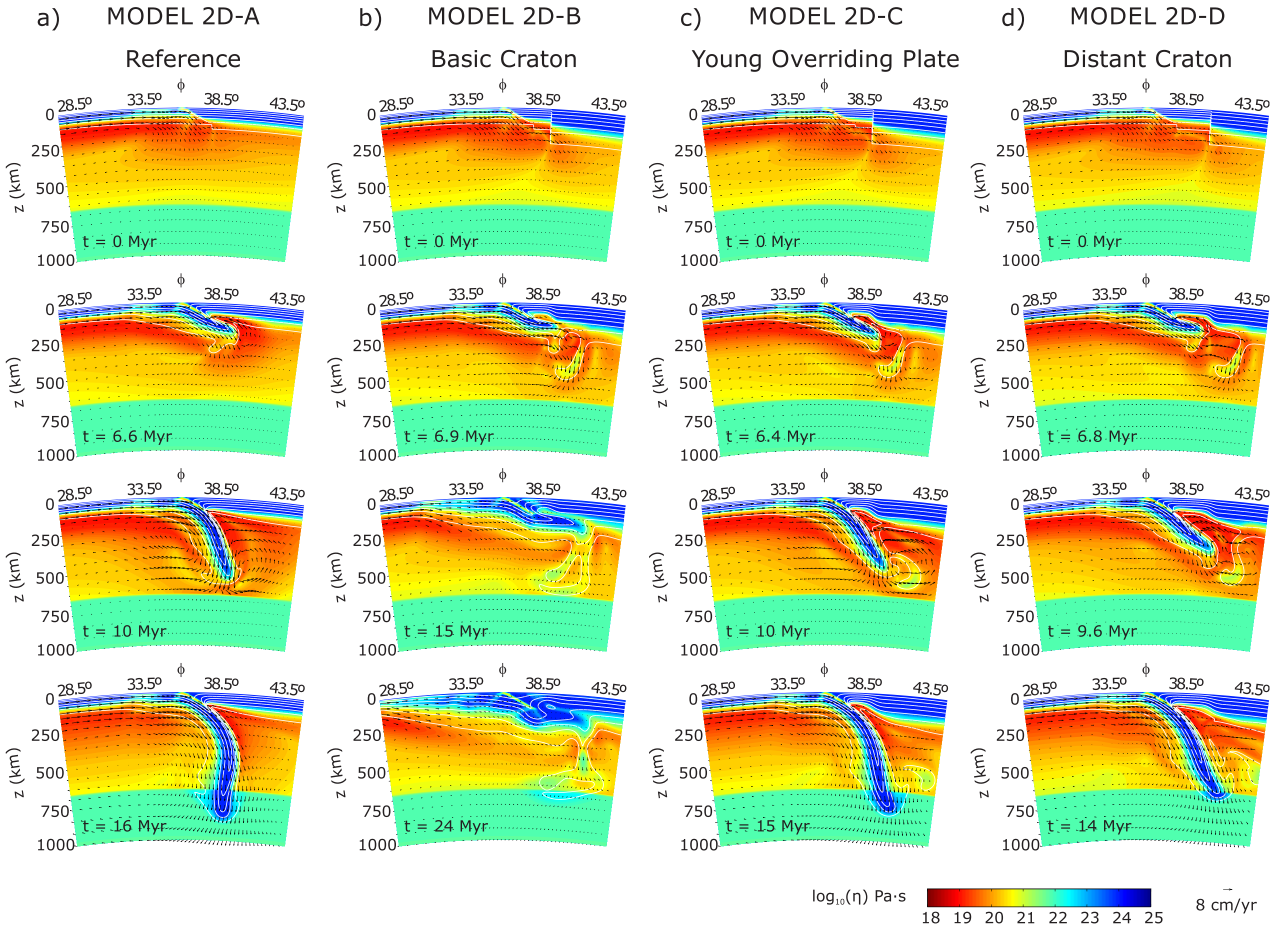

Figure 2. Examples of slab evolution for 2-D kinematically driven exploratory models. Model 2D-A is the reference model, with no craton. Model 2D-B is the same as 2D-A with craton located 3° from the trench: example of a coupled model result. Model 2D-C is the same as model 2D-B but with a younger overriding plate (70 Myr versus 85 Myr): example of an uncoupled model result, but with shallower slab dip than the reference model. Model 2D-D is the same as model 2D-B but with the craton located 4° (~440 km) from the trench: normal-dip subduction occurs if the craton is too far from the trench. A summary of all exploratory 2-D kinematic models is given in Table S2.

because they have less negative buoyancy and are mechanically weaker (i.e., easier to unbend), and therefore provide less resistance to the increased suction in the mantle.

To illustrate the range of behaviors and parameters contributing to flat slab subduction, Figure 2 shows snap-shots in time of four 2-D models (additional tests are shown in supporting information Figures S1–S3). Model 2D-A, with no craton and a relatively old overriding plate (85 Myr or Z_T=118 km) is the reference model. It shows a low slab dip, but no coupling between the slab and the overriding plate. In contrast, coupling is predicted to occur in Model 2D-B, which includes cratonic lithosphere located at a distance of 3° (~330 km) from the trench. In contrast, at a larger distance of 4° transient shallowing of the slab is observed, but it does not become coupled to the overriding plate (compare Model 2D-B and 2D-D).

The 2-D simulations also demonstrate that the thickness of the overriding plate located between the trench and the craton, affects whether slab flattening occurs beneath the craton. In Model 2D-C the overriding plate is relatively thin (age 70 Myr or Z_T=107 km) compared to Model 2D-B, and in this case there is no coupling to the craton. However, for relatively thin overriding plates, young subducting lithosphere (~30 Myr) will couple with the craton (compare Models 2D-C and 2D-G, Figures 2c and S1c). Finally, slab-craton coupling occurs more readily for thicker cratons (Z_T=200 km; Model 2D-B) than for thinner cratons (Z_T=175 km; Model 2D-H).

Therefore, from the 2-D models we conclude that slab flattening is favored by overriding plate structure that includes: trench-craton distances of less than ~350 km, thicker cratons (200 km), and older lithosphere between the trench and craton (85 Myr). We therefore use these parameters in the 3-D kinematic and dynamic models.

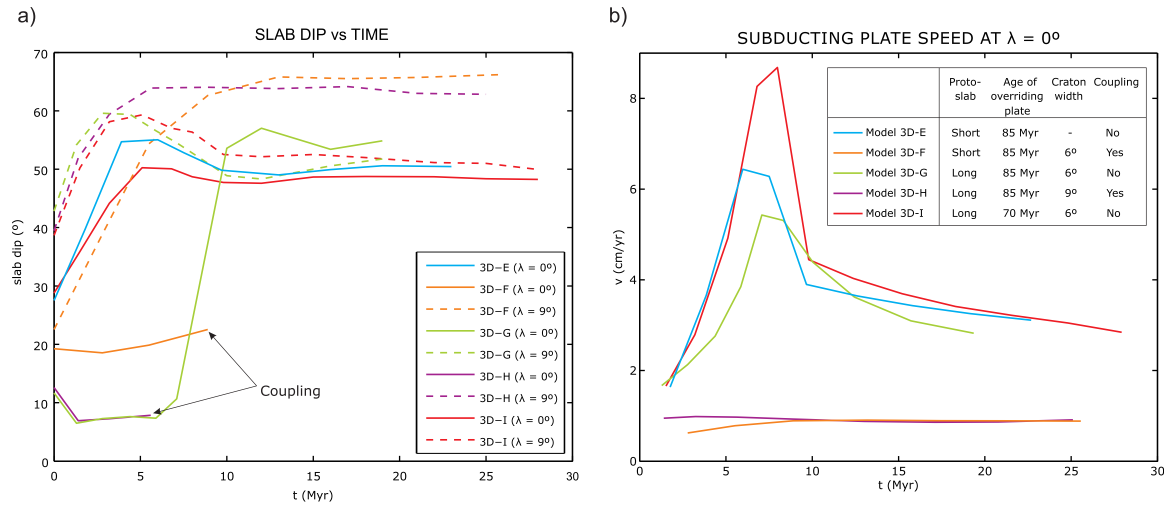

Figure 3. Time-evolution of dynamically driven 3-D models at the slab model center (latitude $\lambda = 0°$) and model edge ($\lambda = 9°$). Blue solid line stands for the reference model (Model 3D-E) with no craton. (a) Slab dip below cratonic (solid lines) and noncratonic regions (dashed lines). Slab dip is measured at depth range 100–200 km beneath the overriding plate. (b) Average velocity at the surface of the subducting plate. All models have an initially slow subduction velocity as the central portion of the proto-slab is pulled up toward the craton. In models with a subsequent increase in subduction velocity, this change in velocity reflects steepening of the slab. See also the slab evolution movies in supporting information.

We next used 3-D kinematic models to investigate the effect of craton width (6°, 9° and 12°) on slab/craton-coupling (supporting information Figures S4–S6). Unlike the 2-D models, the variation in overriding plate structure along-strike introduces a variation in the forces operating on the slab and changes the necessary conditions for creating a fully coupled flat slab. Specifically, we found that very wide cratons (12°) were necessary to cause slab/craton-coupling by inhibiting both poloidal and lateral flow into the central region of the slab. However, even this coupling was focused only in the central 6° of the craton, while the slab continued to slowly sink into the mantle in the adjacent regions (see cross section for later times in Figure S6).

Finally, note that for narrower cratons (6° or 9°) the slab flattens, but does not couple to the overriding plate. The dependence on the craton width in these 3-D kinematically driven models illustrates how the slab pull force, from the slab adjacent to the craton, overcomes the enhanced suction force beneath the craton. In other words, if the ratio of slab width adjacent to the craton to that beneath the craton is sufficiently large, the slab may not couple to the craton unless additional mechanisms are present.

3.2. Three-Dimensional Dynamically Driven Models

We begin with a simulation of a reference model (Model 3D-E) with no craton, a subducting plate of 50 Myr and an overriding plate of 85 Myr (Z_T=118 km). We note that this model is initiated with a "short" proto-slab taken from the 6.1 Myr time-step of the kinematic Model 3D-A (see Tables 1 and S3). The initial dip of the slab is uniform along strike and remains so for the duration of the simulation (blue line in Figure 3a). The time evolution of subduction is characterized by an initial stage of shallow subduction (~30°) during which the subduction rate is slow (~2 cm/yr), followed by rapid slab steepening (increased slab pull force) and increasing subduction rate (>6 cm/yr), and finally normal-dip (~50°) subduction at a slower subduction rate (~4–3 cm/yr) due to interaction with the more viscous lower mantle (blue line in Figure 3b).

Next we present Model 3D-F with the same simulation parameters as the reference model, and a craton in both the kinematic model used to make the proto-slab (Model 3D-Ba) and the dynamic model (Model 3D-F). The western edge of the craton is located at a distance of 3° (~330 km) from the trench and has a latitudinal extent (width) of 6° (~660 km) and a thermal thickness of Z_T=200 km (HSCM age of 235 Myr). In the kinematic model the protoslab has already started to shallow beneath the fore-arc in the cratonic region (Figure 5a). Alternatively, we could have used a kinematic model without a craton to form the proto-slab and then overwritten the overriding plate thermal structure to impose the craton before starting the dynamically driven portion of the model. While this alternative approach may be a stronger test of the ability of the craton to induce upward suction of the slab, we have chosen not to use it for two reasons. First, as described in the introduction, we already know that a thick overriding plate can cause a steep proto-slab to shallow. Second, it is a somewhat unrealistic/artificial initial condition because in the "real" setting the

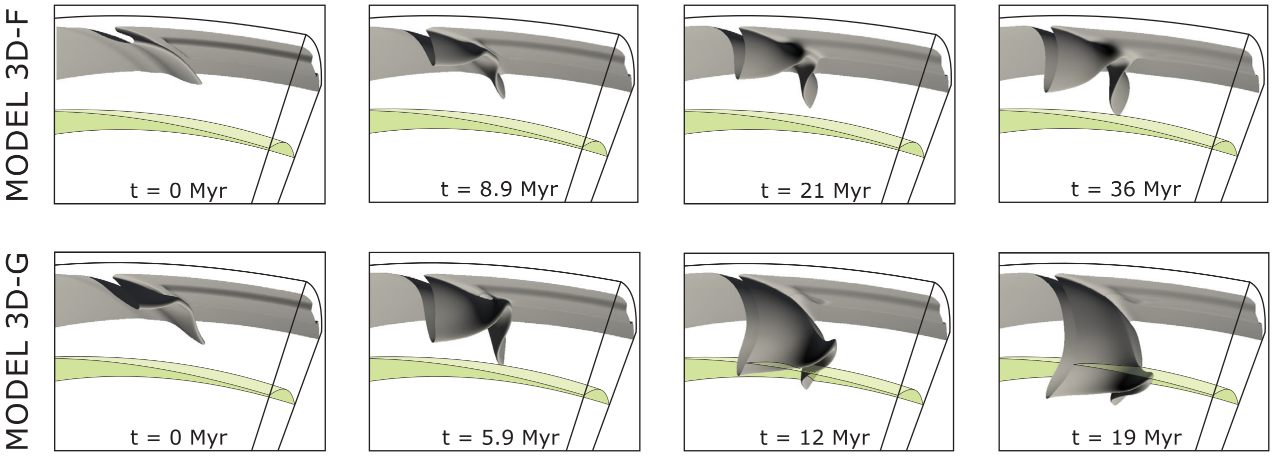

Figure 4. 3-D images for Model 3D-F (permanent coupling) and Model 3D-G (transient flattening) at different times showing the contorted geometry of the slab due to along-trench variable hydrodynamic suction induced by the presence of the craton, which makes the mantle wedge smaller and cooler (more viscous). The slab and overriding plate are represented by the isosurface with a temperature of 900°C. The green surface represents the boundary between upper and lower mantle at 670 km depth.

craton would already exist, and the initial shape of the slab would be affected by it. In addition, initiation of subduction likely requires imposed convergence [e.g., *Gurnis et al*., 2004], that is, subduction initiation does not occur due to slab-pull alone. Therefore the use of a kinematic boundary condition to create the proto-slab in the presence of the craton is a more self-consistent approach to modeling the interaction of the subducting plate with the craton.

At the start of the simulation for Model 3D-F the short proto-slab has a nearly uniform shallow dip of 19–23° and has just reached beneath the front edge of the craton (Figures 4 and 5a). After only 3 Myr of dynamically driven subduction there is a significant reduction of subducting plate velocity to about 0.5 cm/yr (orange line, Figure 3) without the subsequent increase in velocity as was observed in the reference model with no craton. In addition, complete coupling between the slab and the craton occurs by 8.9 Myr (Figures 4, 5a, 6 and supporting information Movies S1–S3). In contrast, adjacent to the craton, the slab steepens to dips of up to 65° and sinks to 250 km depth by 8.9 Myr. However, the available negative slab buoyancy from these steep slab sections is not enough to prevent continuous subcratonic slab shallowing, which leads to permanent coupling. The strong suction beneath the craton is partially enhanced by the decrease in subduction rate, which through the nonlinear viscosity leads to higher viscosity in the mantle wedge. Throughout the simulation the highly contorted shape of the slab produces what appears to be a slab gap in the region beneath the craton (Figure 4).

The competing effects of the slab-pull and the hydrodynamic suction is further illustrated by considering Model 3D-G, which has the same parameters as the reference model and Model 3D-F, except that a longer proto-slab (taken from the 8.1 Myr time-step of kinematic model Model 3D-Ba) is used to drive subduction. In this case the proto-slab has an initial dip of ~12° beneath the craton which increases up to ~45° at the

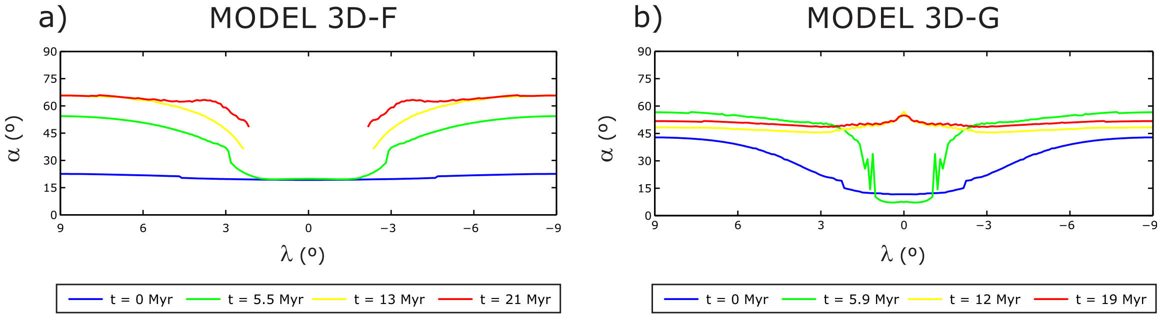

Figure 5. Along-trench slab dip, computed at a depth range 100–200 km beneath the overriding plate at different times for models 3D-F and 3D-G. Note initial shallowing of the central portion of the slab at 5.5 Myr for Model 3D-F and 5.9 Myr Model 3D-G and. The missing section of the curves at 13 and 21 Myr for Model 3D-F denotes the region where the slab is fully coupled to the overriding plate. Note that the colors represent different times in the two models shown (see legend).

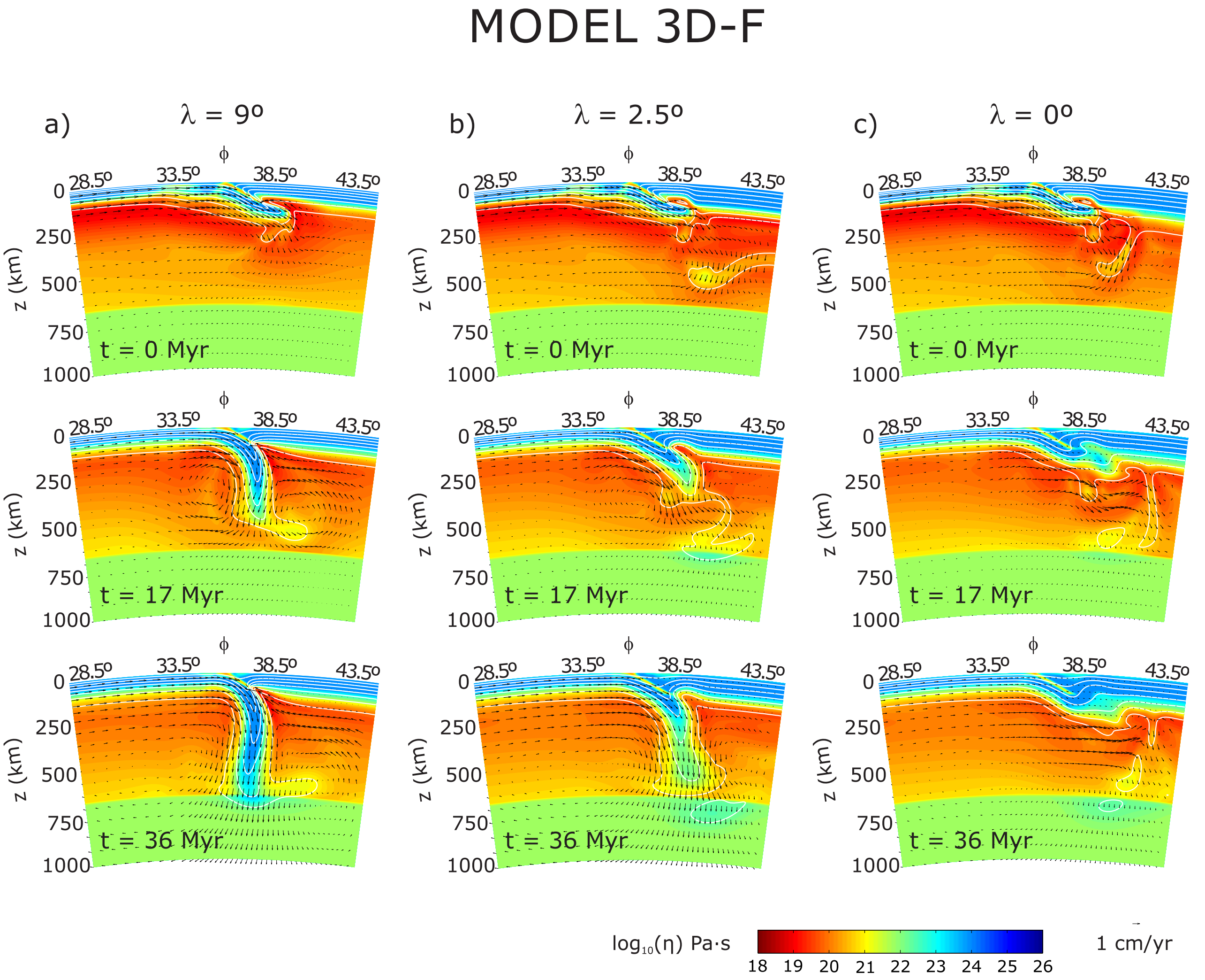

Figure 6. Vertical trench-perpendicular cross sections for Model 3D-F across normal (left) and cratonic (center and right) lithosphere at different time steps. Viscosity structure (colormap), temperature distribution (isotherms every 200 °C) and velocity field (arrows) are shown.

edge of the modeled region. In the regions without a craton, the evolution of the slab is similar to the reference model (Model 3D-E): rapid steepening to a dip of ∼60°, and a similar variation in subduction rate with time, although with a smaller peak subduction rate of 5.5 cm/yr during slab steepening (Figures 3–5). In contrast, in the central portion of the slab beneath the craton, the slab shallows from ∼12° to almost 7° over a narrow region (1° N to 1° S) (Figure 5b).

As the simulation proceeds the flattened portion of the slab beneath the central region of the craton sinks vertically into the mantle without rotating. This sinking process preserves the flattened shape at the tip of the slab as it sinks through the transition zone (Figures 4 and 7), and is a significant difference compared to the behavior observed in 2-D kinematic models C and D (Figure 2) in which the slab pivots (rotates) to a steep slab dip as it decouples from the craton.

The difference in behavior of the slab beneath the craton compared to regions with no craton leads to a highly contorted shape for the slab. After about 8 Myr of evolution, the steeper portions (no craton) are sinking into the lower mantle while the slab is subducting flat beneath the central part ($\lambda=0°$) of the craton (Figures 4, 7, and 8 and supporting information Movies S4–S6). The contorted shape of the slab is due to the surrounding northern and southern portions of the slab progressively pulling down the central part of the slab under the craton. This in turn leads to decoupling of the slab from the overriding plate during sustained subduction.

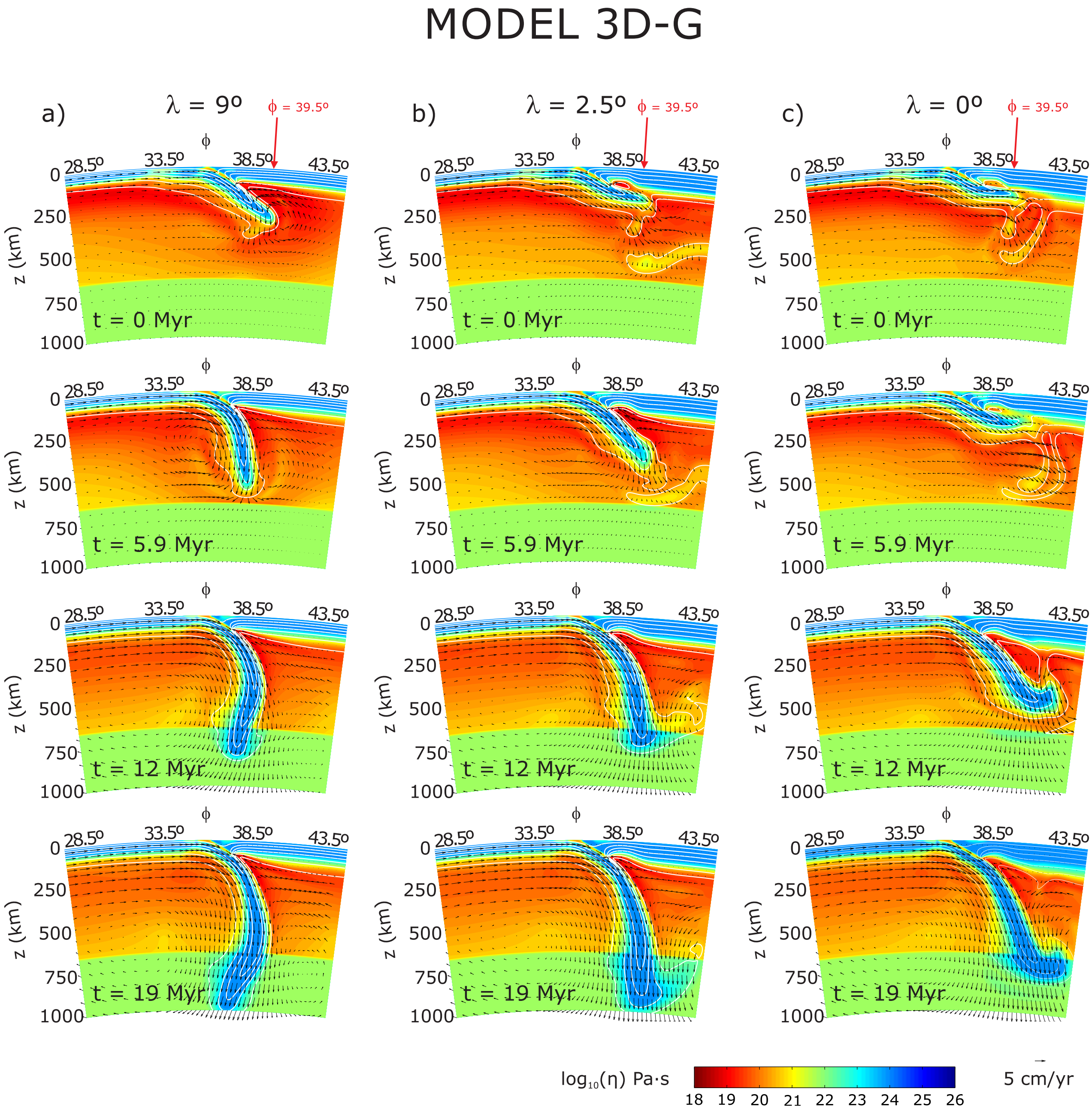

Figure 7. Vertical trench-perpendicular sections for Model 3D-G beneath (left) normal and (middle and right) cratonic lithosphere at different times. Same representation as in Figure 6, except for the different velocity scale used. Cold and thick cratonic lithosphere causes increased hydrodynamic suction and shallower slab dip beneath the central portion of the craton, while adjacent steep slabs continue to pull the subducting plate into the mantle.

Because decoupling of the slab from the craton occurs through first steepening of the north and south portions and then vertical sinking of the most central part, the mantle enters the space between the craton and the slab through a lateral flow from the north and the south (Figure 8). This lateral flow is accompanied by a focused region of upwelling at the apex of the 3-D mantle wedge that migrates to the center of the slab from both the north and the south (Figures 8 and 9). Such a migrating region of upwelling (reaching maximum values of about 4 cm yr^{-1}) could be a source for ultramafic/mafic melts in the mantle and volcanism at the surface, which tracks the decoupling of the slab in the subsurface.

The final modeled stage after slab/craton decoupling is characterized by normal to steeply dipping subduction (Figures 3, 5, and 7). It is worth remarking that the deepest part of the slab, which is sinking into the lower mantle (Figure 4), is the most contorted part, thus indicating that the present-day geometry of deep slabs may preserve evidence for earlier interaction of the slab with the overriding plate. In contrast, the long-term geometry of the upper mantle slab is characterized by increasing homogeneity of slab geometry, due to accumulated slab buoyancy.

Therefore, Model 3D-G with a longer proto-slab (more negative slab buoyancy) leads to a different mode of flat slab subduction, in which the slab interacts with the craton, but does not become permanently coupled. It is important to point out that even though the proto-slab in this model starts out with a shallower dip than the short proto-slab of Model 3D-F, this initial condition does not dictate the subsequent dynamics. Instead, it is the additional slab pull and dynamic weakening of the mantle wedge that acts to decouple the slab. Such transient flattening episodes are inferred for many tectonic histories, as discussed in the introduction.

Additional dynamically driven 3-D simulations were conducted to test the effect of increasing the width of the cratonic area (Model 3D-H) and reducing the age (and therefore the thermal thickness) of the noncratonic portion of the overriding plate (Model 3D-I). For Model 3D-H the increased wedge suction of the wider craton is enough to counteract the increased negative buoyancy from the longer proto-slab and results in a fully coupled flat slab similar to Model 3D-F (purple lines in Figure 3). In contrast, as predicted by the kinematic models, a warmer overriding lithosphere (Model 3D-I) causes a reduction of hydrodynamic suction because of lower viscosity in the mantle wedge, and therefore steeply dipping subduction develops faster and with a higher subduction velocity than in Model 3D-G (red lines in Figure 3). These results are consistent with the behavior inferred from the 2-D and 3-D kinematic models.

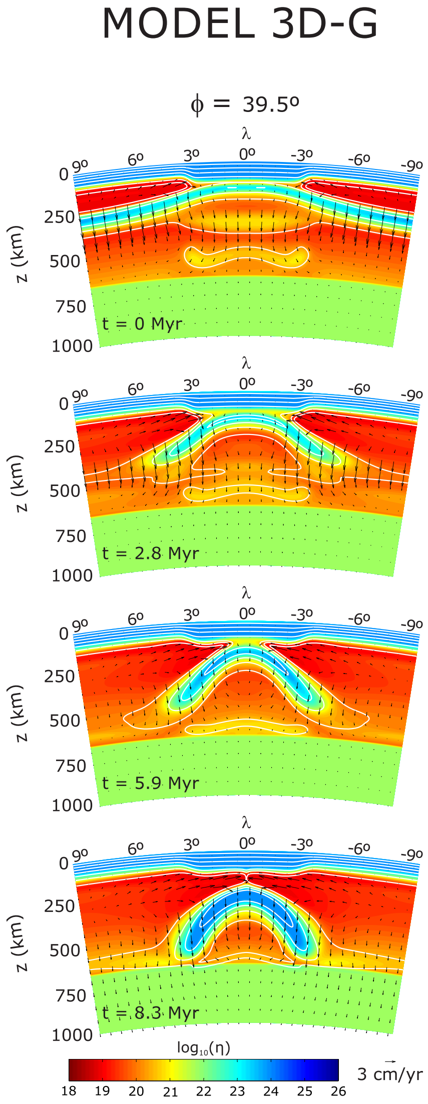

Figure 8. Vertical trench-parallel section for Model 3D-G across mantle wedge (longitude 39.5°) at different times. Viscosity structure, temperature distribution and velocity field are shown (same as in Figure 6). Note that the central flat region of the slab remains flat as it sinks into the mantle and flow enters expanding mantle wedge from the north and south.

4. Discussion

As discussed in the introduction, there are several factors that likely work together to cause flat slabs. Our models are focused only on the effects of a cratonic region in the overriding plate close to the subduction zone. Therefore, our models can not address the added effects of trench rollback or trenchward motion of the overriding plate. In addition, our models are designed to consider the central portion of a long subduction zone and thus also do not include the effect of toroidal flow around a slab edge, which may also induce slab flattening through enhanced trench roll-back [*Schellart et al.*, 2007]. In the models presented here the difference in relative buoyancy of the subcratonic slab and adjacent segments is due to the length of proto-slab. However, other mechanisms for creating a more buoyant subcratonic slab, such as presence of a buoyant ridge or plateau, or younger lithosphere, could also lead to underplating. Similarly, older subducting lithosphere or longer slab segments would promote the transient flattening mode.

Comparison of the kinematically driven and dynamically driven models results provides further insight into suitability of kinematically driven models for studying slab interactions with the overriding plate and the role of far-field stresses. First, if we compare the kinematic model 3D-Ba to the dynamic model 3D-G, we find that the slab dynamics are the same: transient flattening followed by vertical sinking of a flat slab, and

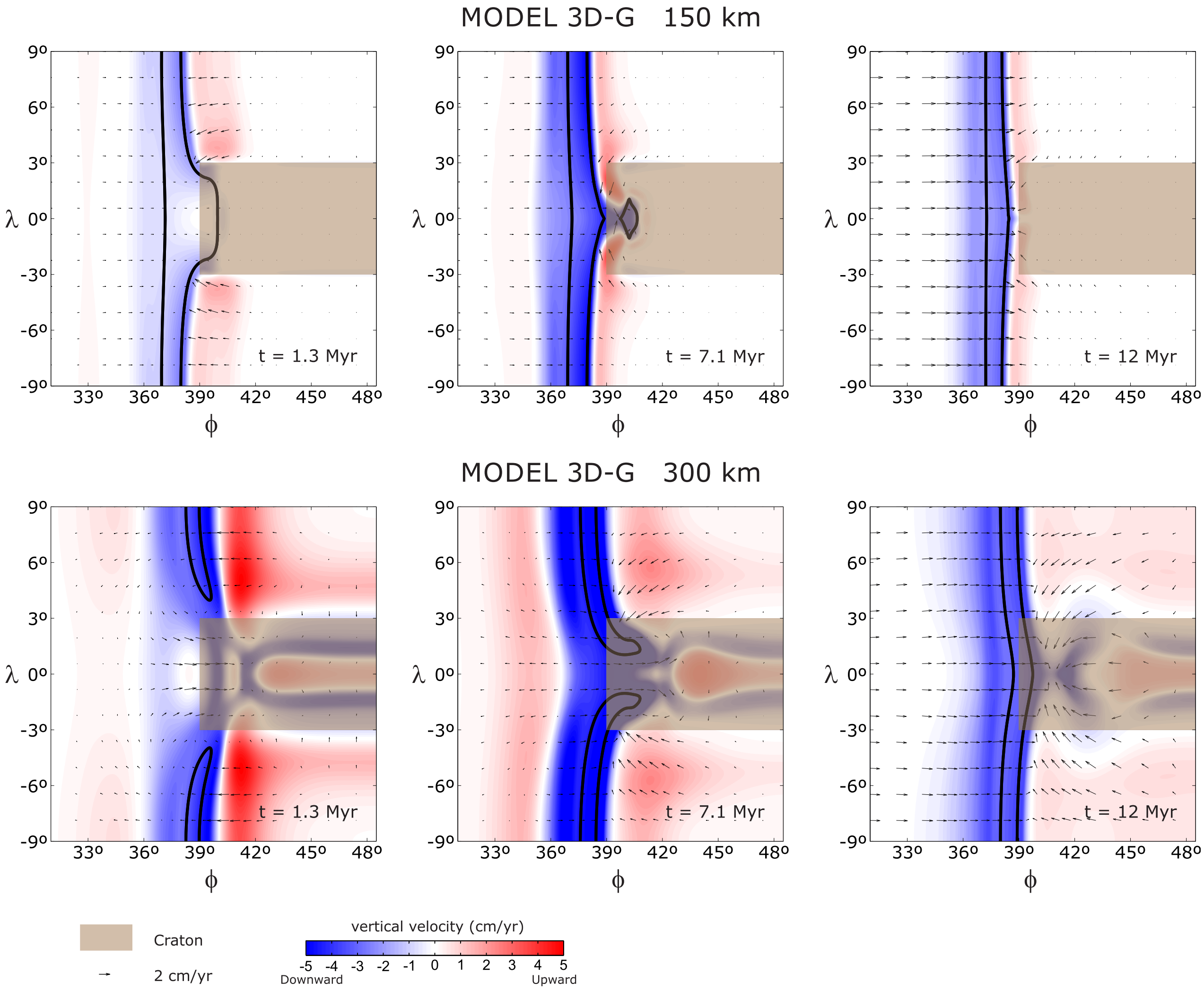

Figure 9. Horizontal sections at 150 and 300 km depths for Model 3D-G. Black contour denotes slab location, represented by the 900°C isotherm. Arrows show horizontal velocity field and colors indicate the vertical (upwelling/downwelling) component of velocity. Note the regions of upwelling flow on either side of the craton, which shifts toward the center as the flat slab section decouples and sinks.

then steep subduction. However, the process is faster in the kinematic model with a constant subduction rate of 8 cm/yr compared to the dynamic model with an average subduction rate about 4 cm/yr (Figure 3b). The faster velocity in the kinematic model should increase suction and favor slab flattening, but this is not what occurs. Instead, the dynamic weakening of the mantle wedge due to the nonlinear viscosity decreases the suction force and counteracts the increased suction due to a faster subduction rate. This suggest that any extra push force due to the applied kinematic boundary condition does not strongly affect the overall dynamics, and as long as the degree of dynamic weakening is sufficient, the kinematic models are a good tool for rapidly exploring model behavior. Second, this result also shows that far-field stresses, such as enhanced ridge push, that act to accelerate subduction relative to the slab-related forces could make flat slab subduction more difficult. This is further illustrated by noting that a wide craton (12°) is necessary to create a coupled flat slab for the kinematic models, while a narrower craton (6°) is sufficient for dynamically driven models.

An additional simplification of the models is that we do not include compositional density or rheology of the craton. Including compositional dependence of rheology would lead to a weaker crust (quartz-rich) but a stronger on the lithosphere (dryer, more mafic), which would enhance suction and slab flattening, but shield the weak crust from the deeper deformational processes. Including compositional buoyancy would bring the overriding lithosphere into isostatic balance. In the present models the weight of the cold/thick craton creates a slight positive pressure beneath the craton. Bringing the overriding plate into isostatic balance by adding lower density crustal material and depleted (less dense) cratonic lithospheric mantle [*Fullea et al*., 2012] would remove this laterally variable positive pressure. However, future models are needed to fully assess the effect of compositional rheology and buoyancy.

One important condition of the model design is that the dynamic models are initiated with a short proto-slab formed in the presence of the craton, and so we model the interaction of the slab and craton early in the subduction process, before the slab penetrates deep into the upper mantle. One can imagine that if the slab and craton become close in proximity only after the slab had been subducting for some time (i.e., reaching the lower mantle), then the slab dip would decrease, but the degree of slab flattening would be smaller because there is greater slab pull with which to counteract the increased suction beneath the craton, as illustrated by the difference in behavior of Models 3D-F and 3D-G. In this case, other factors such as the presence of more buoyant material (an aseismic ridge or an oceanic plateau) or trench rollback or trench-ward motion of the overriding plate (with subduction erosion) might be needed to generate a shallow slab, that is then also close enough to the craton to interact with it. Such a scenario has been proposed for the Laramide flat slab [*Jones et al*., 2011].

4.1. Implications for Surface Observations Related to Flat Slabs

The process of decoupling the transient flat slab from the craton makes predictions about the expected pattern of volcanism and/or deformation to accompany the decoupling process. First, volcanism would cease while the flat slab is coupled to the overriding plate due to the lack of hot mantle asthenosphere above the slab. Our models predict that the pattern of volcanism is expect to migrate from the edges of the craton toward the center along strike as the flat slab sinks vertically into the mantle and flow migrates in from the edges of the craton (Figures 8 and 9). This pattern of spatially converging volcanism is inferred for the post-Laramide flat slab in the western U.S. from the age progression of basaltic volcanism [*Johnson*, 1991; *Humphreys*, 1995]. One would also expect vertical motion of the craton to follow a similar spatial pattern and be recorded in the formation and deposition in basins followed by uplift and exhumation [*Jones et al*., 2011].

4.2. Implications for Interpretation of Seismic Images

In addition to providing insight into the physical mechanism and degree of slab flattening that can occur due to the presence of cratonic lithosphere, these models make predictions about how these slabs may appear in seismic images of the mantle. First, in the case of transient slab flattening, one would expect to see highly contorted slab shapes in the upper mantle soon after the end of the flat slab episode. Return to a more homogeneous slab shape in the upper mantle will occur after longer times, but the signature of the previous flat slab episode may be preserved in the deeper structure of the slab. Second, in the case of permanent underplating a slab gap will occur beneath the craton. Eventually, this gap could lead to tearing of the adjacent sections of subducting plate or tearing of the underplated section along-strike and initiation of a new subduction zone. Such scenarios complicate the interpretation of seismic images as time progresses from the initial underplating event. The important point however is that not every slab gap must be due to a detached slab, but instead could also be due to an underplated flat slab.

For example, In South America, recent seismic data demonstrate that the flat slab section beneath Peru is actively tearing and reestablishing subduction behind this tear [*Knezevic Antonijevic et al*., 2015]. It is too soon to know if the flat slab section will become permanently underplated (as inferred for the Siletzia flat slab) or if the flat subduction will be transient as the slab is pulled into the mantle by the adjacent sections of the slab. Given the narrow extent of the Nazca ridge and large region of normally subducting plate to either side [*Knezevic Antonijevic et al*., 2015], the negative buoyancy of the adjacent regions should be sufficient to pull the flat-slab section down [*Arrial and Billen*, 2013]. However this prediction also depends on the mechanical coupling of the flat slab to the overriding plate.

In North America, a well-known example of transient flat subduction is the Farallon slab during the Laramide orogeny [e.g., *Humphreys*, 1995; *Jones et al*., 2011]. This previously flat slab now resides in the lower mantle and is imaged with a near-horizontal dip at North American latitudes [e.g., *Ritsema et al*., 2004; *Sigloch*, 2011]. The magmatic record at the surface suggests that the flat slab decoupled from the overriding plate starting in both the north and south, and progressed toward the middle of the slab [*Johnson*, 1991; *Humphreys*, 1995]. Both the flat geometry of the slab in the lower mantle and the spatial progression of volcanism are consistent with our model predictions for a transient flat slab that is vertically pulled down (without rotating) by the adjacent nonflat sections of the lithosphere (Model 3D-G).

The unprecedented increase in data resolution beneath North America due to the US Array has also lead to a number of new seismic observations of the lithosphere and upper mantle related to subduction along the Cascadia Arc. One such example is a circular downwelling beneath north-eastern Oregon known as the Wallowa anomaly [*Gao et al*., 2011; *Schmandt and Humphreys*, 2011; *Darold and Humphreys*, 2013], which is interpreted to be related to a previous flat slab event occurring during the emplacement of the Siletzia Terrane (an oceanic plateau) in present-day Oregon [*Wells et al*., 2014]. This flat slab section also occurred beneath the edge of the Wyoming craton, consistent with our prediction that cratonic lithosphere can promote flat slab subduction. Seismic images of the narrow downwelling beneath the north-east corner of Oregon are interpreted as resulting from destabilization of the underplated slab due to inflow of hot plume material related to the Yellowstone hotspot [*Darold and Humphreys*, 2013]. Until this recent destabilization event (~16 Ma) this section of the Cascadia subduction zone may have appeared as a slab gap [see e.g., *Sigloch*, 2011, Figure 3], as predicted by our permanent underplating model (Model 3D-F).

4.3 Implications for the Evolution of Cratons

Several lines of observational evidence suggest that subducting slabs can become permanently coupled to continents: images of layered structures in the cratons are interpreted as preserving underplated slabs [e.g., *Simon et al*., 2007; *Canil*, 2008; *Lee et al*., 2011] and slab-derived eclogites brought to the surface in kimberlite pipes [*Shirey et al*., 2013 and references therein) are interpreted as sampling subducting slabs that have been incorporated into the craton. Indeed, underplating of cratons may have an important role in stabilizing cratons by adding strong, mafic material to the base of the lithosphere [*Yuan and Romanowicz*, 2010]. The results of our models suggest that cratons play an active role in the underplating process by creating more favorable dynamical conditions for underplating buoyant subducting lithosphere. For example, in the case of oceanic plateau subduction, the suction effect of the craton could counter-balance the effects of eclogitization of the crust making it more common to underplate plateaus under cratons.

5. Conclusions

Using 3-D fully dynamic models of subduction we have shown that slab flattening can occur beneath cold/thick cratons as a result of an increase in hydrodynamic suction in the mantle wedge beneath the craton relative to surrounding regions with thinner lithosphere. The degree of coupling is larger for small negative buoyancy of subducting lithosphere, older and thicker overriding plates, and wider and thicker cratons. In addition, the trench-craton distance must be less than a critical distance to have an impact on slab evolution. For the models presented here the critical distance is about 3.5°, but the exact value likely depends on other parameters in the model such as the viscosity and dip of the PBSZ. We also find that there are two modes of slab flattening: (1) *permanent underplating* (Model 3D-F) occurs when the suction is sufficient to fully couple the subducting plate to the overriding lithosphere, and (2) *transient flattening* (Model 3D-G) occurs when there is sufficient negative-slab buoyancy available along strike (longer/more slab adjacent to craton) to overcome the increased suction on the slab beneath the craton.

While episodes of transient flattening or permanent underplating of slabs have generally been attributed to the subduction of a buoyant oceanic plateau or episode of rapid trench roll-back, we have shown that the cratons themselves play an active role in this process. The implication of the models presented here is that underplating of slabs does not happen just anywhere, but rather occurs preferentially under cratons because the hydrodynamic suction is higher in these locations compared to thinner continental lithosphere. This result therefore suggests that cratons have a built-in regeneration mechanism because, unlike thinner parts of continents, they are more likely to be underplated by pieces of the subducting plate. This is a testable hypothesis: global geological observations can be analyzed for correspondence of underplated or accreted plateaus and their proximity to cratons. Future models, including subducting oceanic plateaus and the basalt-eclogite transition, can evaluate this interaction by analyzing the dynamics for oceanic plateaus of various thickness and size.

Acknowledgments

The data displayed in this paper were computed with the free software CitcomS (http://www.geodynamics.org/cig/software/citcoms). Model results were postprocessed and represented (Figures 2, 3, 5–9, S1–S6, and Movies S2, S3, S5, and S6) using commercial code Matlab (www.mathworks.com/products/matlab/). Figure 4 and Movies S1 and S4 were produced using public domain software ParaView (http://www.paraview.org). This work was supported by Spanish Ministry of Economy and Competitiveness projects CGL2012-37222 and CGL2014-58821-C2-1-R. M.I. Billen acknowledges support from NSF grants 6877321 and 0748818. We thank the Editor and Leland O'Driscoll, Maxim Ballmer and an anonymous reviewer for their thoughtful and constructive comments.

References

Anderson, M. L., P. Alvarado, G. Zandt, and S. Beck (2007), Geometry and brittle deformation of the subducting Nazca Plate, Central Chile and Argentina, *Geophys. J. Int.*, *171*(1), 419–434.

Antonijevic, S. K., L. S. Wagner, A. Kumar, S. L. Beck, M. D. Long, G. Zandt, H. Tavera, and C. Condori (2015), The role of ridges in the formation and longevity of flat slabs, *Nature*, *524*, 212–215, doi:10.1038/nature14648.

Arredondo, K., and M. Billen (2014), Dynamic linkages between the transition zone & surface plate motion in 2D models of subduction, Abstract DI33A-2216 presented at 2014 Fall Meeting, AGU, San Francisco, Calif.

Arrial, P.-A., and M. I. Billen (2013), Influence of geometry and eclogitization on oceanic plateau subduction, *Earth Planet. Sci. Lett.*, *363*, 34–43.

Artemieva, I. M. (2006), Global 1°×1° thermal model TC1 for the continental lithosphere: Implications for lithosphere secular evolution, *Tectonophysics*, *416*(1-4), 245–277.

Betts, P. G., L. Moresi, M. S. Miller, and D. Willis (2015), Geodynamics of oceanic plateau and plume head accretion and their role in Phanerozoic orogenic systems of China, *Geosci. Frontiers*, *6*(1), 49–59.

Billen, M. I., and G. Hirth (2007), Rheologic controls on slab dynamics, *Geochem. Geophys. Geosyst.*, *8*, Q08012, doi:10.1029/2007GC001597.

Blackwell, D., and M. Richards (2004), Geothermal Map of North America, AAPG Map, scale 1:6,500,000, Product Code 423.

Bruns, T. R. (1985), Tectonics of the Yakutat block, an allochthonous terrane in the northern Gulf of Alaska, *Rep. 85-13*, 112 pp., U.S. Geol. Surv., Menlo Park, Calif.

Canil, D. (2008), Canada's craton: A bottoms-up view, *GSA Today*, *18*(6), 4–10.

Capitanio, F. A., D. R. Stegman, L. N. Moresi, and W. Sharples (2010), Upper plate controls on deep subduction, trench migrations and deformations at convergent margins, *Tectonophysics*, *483*(1-2), 80–92.

Cizkova, H., J. van Hunen, A. P. van den Berg, and N. J. Vlaar (2002), The influence of rheological weakening and yield stress on the interaction of slabs with the 670 km discontinuity, *Earth Planet. Sci. Lett.*, *193*(3-4), 447–457.

Cloos, M. (1993), Lithospheric buoyancy and collisional orogenesis: Subduction of oceanic plateaus, continental margins, island arcs, spreading ridges, and seamounts, *Geol. Soc. Am. Bull.*, *105*(6), 715–737.

Cross, T. A., and R. H. Pilger (1982), Controls of subduction geometry, location of magmatic arcs, and tectonics of arc and back-arc regions, *Geol. Soc. Am. Bull.*, *93*, 545–562.

Currie, C. A., and C. Beaumont (2011), Are diamond-bearing Cretaceous kimberlites related to low-angle subduction beneath western North America?, *Earth Planet. Sci. Lett.*, *303*(1-2), 59–70.

Darold, A., and E. Humphreys (2013), Upper mantle seismic structure beneath the Pacific Northwest: A plume-triggered delamination origin for the Columbia River flood basalt eruptions, *Earth Planet. Sci. Lett.*, *365*, 232–242.

Espurt, E., F. Funiciello, J. Martinod, B. Guillaume, V. Regard, C. Faccenna, and S. Brusset (2008), Flat subduction dynamics and deformation of the South American plate: Insights from analog modeling, *Tectonics*, *27*, TC3011, doi:10.1029/2007TC002175.

Fullea, J., S. Lebedev, M. R. Agius, A. G. Jones, and J. C. Afonso (2012), Lithospheric structure in the Baikal–central Mongolia region from integrated geophysical-petrological inversion of surface-wave data and topographic elevation, *Geochem. Geophys. Geosyst.*, *13*, Q0AK09, doi:10.1029/2012GC004138.

Gao, H., E. D. Humphreys, H. Yao, and R. D. van der Hilst (2011), Crust and lithosphere structure of the northwestern U.S. with ambient noise tomography: Terrane accretion and Cascade arc development, *Earth Planet. Sci. Lett.*, *304*(1-2), 202–211.

Garel, F., S. Goes, D. Davies, J. H. Davies, S. Kramer, and C. Wilson (2014), Interaction of subducted slabs with the mantle transition-zone: A regime diagram from 2-D thermo-mechanical models with a mobile trench and an overriding plate, *Geochem. Geophys. Geosyst.*, *15*, 1739–1765, doi:10.1002/2014GC005257.

Gerya, T. V., D. Fossati, C. Cantieni, and D. Seward (2009), Dynamic effects of aseismic ridge subduction: Numerical modelling, *Eur. J. Mineral.*, *21*(3), 649–661.

Gurnis, M., C. Hall, and L. Lavier (2004), Evolving force balance during incipient subduction, *Geochem. Geophys. Geosyst.*, *5*, Q07001, doi:10.1029/2003GC000681.

Gutscher, M.-A., J. L. Olivet, D. Aslanian, J.-P. Eissen, and R. C. Maury (1999), The "lost Inca Plateau": Cause of flat subduction beneath Peru?, *Earth Planet. Sci. Lett.*, *171*, 335–341.

Gutscher, M.-A., W. Spakman, H. Bijwaard, and E. R. Engdahl (2000), Geodynamics of flat subduction: Seismicity and tomographic constraints from the Andean margin, *Tectonics*, *19*(5), 814–833.

Hager, B. H. (1984), Subducted slabs and the geoid: Constraints on mantle rheology and flow, *J. Geophys. Res.*, *86*(B7), 6003–6015.

Holt, A. F., T. W. Becker, and B. A. Buffett (2015), Trench migration and overriding plate stress in dynamic subduction models, *Geophys. J. Int.*, *201*(1), 172–192.

Humphreys, E. D. (1995), Post-Laramide removal of the Farallon slab, western United States, *Geology*, *23*(11), 987–990.

Jadamec, M. A., and M. I. Billen (2010), Reconciling surface plate motions with rapid three-dimensional mantle flow around a slab edge, *Nature*, *465*, 338–341.

Johnson, C. M. (1991), Large-scale crust formation and lithosphere modification beneath Middle to Late Cenozoic calderas and volcanic fields, western North America, *J. Geophys. Res.*, *96*(B8), 13,485–13,507.

Jones, C. H., G. L. Farmer, B. Sageman, and S. Zhong (2011), Hydrodynamic mechanism for the Laramide orogeny, *Geosphere*, *7*, 183–201.

Lee, C.-T. A., P. Luffi, and E. J. Chin (2011), Building and destroying continental mantle, *Annu. Rev. Earth Planet. Sci., 39*, 59–90.

Liu, L., and D. R. Stegman (2011), Segmentation of the Farallon slab, *Earth Planet. Sci. Lett.*, *311*(1-2), 1–10.

Liu, L., M. Gurnis, M. Seton, J. Saleeby, R. D. Muller, and J. M. Jackson (2010), The role of oceanic plateau subduction in the Laramide orogeny, *Nat. Geosci.*, *3*(5), 353–357.

Manea, V. C., M. Pérez-Gussinyé, and M. Manea (2012), Chilean flat slab subduction controlled by overriding plate thickness and trench rollback, *Geology*, *40*(1), 35–38.

Martinod, J., F. Funiciello, C. Faccenna, S. Labanieh, and V. Regard (2005), Dynamical effects of subducting ridges: Insights from 3-D laboratory models, *Geophys. J. Int.*, *163*(3), 1137–1150.

Meyer, C., and W. Schellart (2013), Three-dimensional dynamic models of subducting plate-overriding plate-upper mantle interaction, *J. Geophys. Res. Solid Earth*, *118*, 775–790, doi:10.1002/jgrb.50078.

O'Driscoll, L. J., E. D. Humphreys, and F. Saucier (2009), Subduction adjacent to deep continental roots: Enhanced negative pressure in the mantle wedge, mountain building and continental motion, *Earth Planet. Sci. Lett.*, *280*(1-4), 61–70.

O'Driscoll, L. J., M. A. Richards, and E. D. Humphreys (2012), Nazca–South America interactions and the late Eocene–late Oligocene flat-slab episode in the central Andes, *Tectonics*, *31*, TC2013, doi:10.1029/2011TC003036.

Pardo, M., and G. Suarez (1995), Shape of the subducted Rivera and Cocos plates in southern Mexico: Seismic and tectonic implications, *J. Geophys. Res.*, *100*(B7), 12,357–12,373.

Parker, R. L., and D. W. Oldenburg (1973), Thermal model of ocean ridges, *Nature*, *242*, 137–139.

Pérez-Gussinyé, M., A. R. Lowry, J. Phipps Morgan, and A. Tassara (2008), Effective elastic thickness variations along the Andean margin and their relationship to subduction geometry, *Geochem. Geophys. Geosyst.*, *9*, Q02003, doi:10.1029/2007GC001786.

Ritsema, J., H. J. van Heijst, and J. H. Woodhouse (2004), Global transition zone tomography, *J. Geophys. Res. Solid Earth*, *109*, B02302, doi:10.1029/2003JB002610.

Roda, M., A. M. Marotta, and M. I. Spalla (2011), The effects of the overriding plate thermal state on the slab dip in an ocean-continent subduction system, *C. R. Geosci.*, *343*(5), 323–330.

Rodríguez-González, J., A. M. Negredo, and M. I. Billen (2012), The role of the overriding plate thermal state on slab dip variability and on the occurrence of flat subduction, *Geochem. Geophys. Geosyst.*, *13*, Q01002, doi:10.1029/2011GC003859.

Rodríguez-González, J., M. I. Billen, and A. M. Negredo (2014), Non-steady-state subduction and trench parallel flow induced by overriding plate structure, *Earth Planet. Sci. Lett*, *401*, 227–235.

Saleeby, J. (2003), Segmentation of the Laramide slab—Evidence from the southern Sierra Nevada region, *Geol. Soc. Am. Bull*, *115*, 655–668.

Schellart, W. P., J. Freeman, D. R. Stegman, L. Moresi, and D. May (2007), Evolution and diversity of subduction zones controlled by slab width, *Nature*, *446*, 308–311.

Schellart, W. P., D. R. Stegman, and J. Freeman (2008), Global trench migration velocities and slab migration induced upper mantle volume fluxes: Constraints to find an Earth reference frame based on minimizing viscous dissipation, *Earth Sci. Rev.*, *88*, 118–144.

Schellart, W. P., D. R. Stegman, R. J. Farrington, J. Freeman, and L. Moresi (2010), Cenozoic tectonics of western North America controlled by evolving width of Farallon slab, *Science*, *329*, 316–319.

Schmandt, B., and E. Humphreys (2011), Seismically imaged relict slab from the 55 Ma Siletzia accretion to the northwest United States, *Geology*, *39*(2), 175–178.

Shirey, S. B., P. Cartigny, D. J. Frost, S. Keshav, F. Nestola, P. Nimis, D. G. Pearson, N. V. Sobolev, and M. J. Walter (2013), Diamonds and the geology of mantle carbon, *Rev. Mineral. Geochem.*, *75*(1), 355–421.

Sigloch, K. (2011), Mantle provinces under North America from multifrequency P wave tomography, *Geochem. Geophys. Geosyst.*, *12*, Q02W08, doi:10.1029/2010GC003421.

Simon, N. S. C., R. W. Carlson, D. G. Pearson, and G. R. Davies (2007), The origin and evolution of the Kaapvaal cratonic lithospheric mantle, *J. Petrol.*, *48*(3), 589–625.

Skinner, S. M., and R. W. Clayton (2013), The lack of correlation between flat slabs and bathymetric impactors in South America, *Earth Planet. Sci. Lett.*, *371–372*, 1–5.

Stevenson, D. J., and J. S. Turner (1977), Angle of subduction, *Nature*, *270*, 334–336.

Tan, E., E. Choi, P. Thoutireddy, M. Gurnis, and M. Aivazis (2006), GeoFramework: Coupling multiple models of mantle convection within a computational framework, *Geochem. Geophys. Geosyst.*, *7*, Q06001, doi:10.1029/2005GC001155.

Tassara, A., and A. Echaurren (2012), Anatomy of the Andean subduction zone: Three-dimensional density model upgraded and compared against global-scale models, *Geophys. J. Int.*, *189*(1), 161–168.

Tassara, A., H.-J. Götze, S. Schmidt, and R. Hackney (2006), Three-dimensional density model of the Nazca plate and the Andean continental margin, *J. Geophys. Res.*, *111*, B09404, doi:10.1029/2005JB003976.

Turcotte, D. L., and J. Schubert (2002), *Geodynamics*, 2 ed., Cambridge Univ. Press, Cambridge, U. K.

van den Berg, A. P., P. E. van Keken, and D. A. Yuen (1993), The effects of a composite non-Newtonian and Newtonian rheology on mantle convection, *Geophys. J. Int.*, *115*, 62–78.

van der Lee, S., and G. Nolet (1997), Seismic image of the subducted trailing fragments of the Farallon plate, *Nature*, *386*, 266–269.

van Hunen, J., A. P. van den Berg, and N. J. Vlaar (2000), A thermo-mechanical model of horizontal subduction below an overriding plate, *Earth Planet. Sci. Lett.*, *182*(2), 157–169.

van Hunen, J., A. P. van den Berg, and N. J. Vlaar (2002), On the role of subducting oceanic plateaus in the development of shallow flat subduction, *Tectonophysics*, *352*(3-4), 317–333.

Vlaar, N. J. (1983), Thermal anomalies and magmatism due to lithospheric doubling and shifting, *Earth Planet. Sci. Lett.*, *65*(2), 322–330.

Vogt, P. R. (1973), Subduction and aseismic ridges, *Nature*, *241*(5386), 189–191.

Wells, R., D. Bukry, R. Friedman, D. Pyle, R. Duncan, P. Haeussler, and J. Wooden (2014), Geologic history of Siletzia, a large igneous province in the Oregon and Washington Coast Range: Correlation to the geomagnetic polarity time scale and implications for a long-lived Yellowstone hotspot, *Geosphere*, *10*(4), 692–719.

Yuan, H., and B. Romanowicz (2010), Lithospheric layering in the North American craton, *Nature*, *466*, 1063–1068.

Zhong, S., M. T. Zuber, L. Moresi, and M. Gurnis (2000), The role of temperature-dependent viscosity and surface plates in spherical shell models of mantle convection, *J. Geophys. Res.*, *105*(B5), 11,063–11,082.